Title

Winter westerly disturbance dynamics and precipitation in the western Himalaya and Karakoram: a wave-tracking approach

Journal

Theoretical and Applied Climatology, 125(1-2)

ISSN

0177-798X

Authors

Cannon, Forest
Carvalho, Leila MV
Jones, Charles
et al.

Publication Date

2016-07-01

DOI

10.1007/s00704-015-1489-8

Peer reviewed

Theor Appl Climatol
DOI 10.1007/s00704-015-1489-8

ORIGINAL PAPER

Winter westerly disturbance dynamics and precipitation in the western Himalaya and Karakoram: a wave-tracking approach

Forest Cannon[1,2] · **Leila M.V. Carvalho**[1,2] · **Charles Jones**[1,2] · **Jesse Norris**[2]

Received: 7 January 2015 / Accepted: 24 April 2015

Abstract Extratropical cyclones, including winter westerly disturbances (WWD) over central Asia, are fundamental features of the atmosphere that maintain energy, momentum, and moisture at global scales while intimately linking large-scale circulation to regional-scale meteorology. Within high mountain Asia, WWD are the primary contributor to regional precipitation during winter. In this work, we present a novel WWD tracking methodology, which provides an inventory of location, timing, intensity, and duration of events, allowing for a comprehensive study of the factors that relate WWD to orographic precipitation, on an individual event basis and in the aggregate. We identify the relationship between the strength of disturbances, the state of the background environment during their propagation, and precipitation totals in the Karakoram/western Himalaya. We observe significant differences in convective and mechanical instability contributions to orographic precipitation as a function of the relationship between the intensity of WWD and the background temperature and moisture fields, which exhibit strong intraseasonal variability. Precipitation is primarily orographically forced during intense WWD with strong cross-barrier winds, while weaker WWD with similar precipitation totals are observed to benefit from enhanced instability due to high moisture content and temperature at low levels, occurring primarily in the late winter/premonsoon. The contribution of these factors is observed to fluctuate on a per-case basis, indicating important influences of intraseasonal oscillations and tropical-extratropical interactions on regional precipitation.

✉ Forest Cannon
fcannon@geog.ucsb.edu

[1] Department of Geography, University of California, Santa Barbara, Santa Barbara, CA 93106, USA

[2] Earth Research Institute, University of California, Santa Barbara, Santa Barbara, CA, USA

1 Introduction

Water resources in high mountain Asia (HMA) are important for hundreds of millions of people throughout southern and central Asia (Kaab et al. 2012). Recently, numerous studies have been undertaken to evaluate changes in glaciers across the region, as they are important storage reservoirs, which provide water for agriculture, power generation, and human consumption during low-precipitation months (Gardelle et al. 2012; Bookhagen and Burbank 2010; Bolch et al. 2012). In the western Himalaya and Karakoram (KH) and, to a lesser degree, the central Himalaya, winter westerly disturbances are the primary climatic influence during nonmonsoon months (Singh et al. 1995; Lang and Barros 2004; Barlow et al. 2005). The link between the atmosphere and glacial trends has also motivated studies on wintertime climate variability (Archer and Fowler 2004; Bhutiyani et al. 2010; Dimri and Dash 2012; Palazzi et al. 2013). In the KH, an excess of 50 % of the total annual precipitation is delivered by only a few westerly disturbances occurring between the months of December and March (Barros et al. 2006). Winter westerly disturbances (WWD) are characteristically eastward propagating extratropical cyclones (Lang and Barros 2004; Barlow et al. 2005). Their associated frontal systems interact with HMA topography and warm tropical air masses over the Indian subcontinent to produce heavy precipitation in the KH during winter and spring (Ridley et al. 2013).

Precipitation produced by WWD is supplied by advected moisture from the Mediterranean, Red, Persian, and Arabian Seas (Singh et al. 1995; Barlow et al. 2005, Filippi et al. 2014).

Published online: 10 May 2015

Within the convectively stable wintertime environment, precipitation is mechanically forced by air impinging on terrain (Roe 2005). KH orography induces a significant blocking effect thereby modifying regional and large-scale circulation and the distribution of orographic precipitation. The environmental lapse rate ensures that the majority of precipitation within the KH's high topography falls as snow (Immerzeel et al. 2009; Tahir et al. 2011). Snowfall is a primary determinant of glacial mass balance in HMA (Hewitt 2005; Bolch et al. 2012).

WWD are well associated with a baroclinic wave approaching HMA and exhibiting prototypical cold-frontal behavior (e.g., Holton 2004). Lag-composite analysis of WWD events producing heavy precipitation in the KH displays a deep upper-level trough, propagating along a Rossby waveguide (Hoskins and Ambrizzi 1993), stationed several degrees to the west of the KH during the maximum in precipitation and exhibiting vertical tilting (e.g., Cannon et al. 2014, their Fig. 3). Moisture is advected northward along the cold front and into a notch in the KH, which captures and orographically lifts the flow to produce precipitation. Long-term studies in the frequency and intensity of WWD typically analyze upper-level variability of geopotential height over several decades because the deep synoptic trough associated with the cyclone exhibits a distinctive signature. Lang and Barros (2004) identified a significant relationship between 500-hPa geopotential height and heavy precipitation events in the central Himalaya and used this relationship to evaluate WWD activity over several decades of reanalysis. Increased variability of 500-hPa height indicated more frequent troughs and was positively correlated to increased precipitation. Similarly, Cannon et al. (2014) used wavelet-derived synoptic variability of upper-level geopotential height to estimate WWD activity between 1979 and 2010. Their work indicated increasing variability in 200-hPa geopotential height at synoptic scales and gave evidence of increased WWD activity contributing to trends in glacier mass balance across HMA.

Numerous studies found WWD to be significantly influenced by the Madden-Julian Oscillation (Barlow et al. 2005; Hoell et al. 2013), the El Niño Southern Oscillation (Syed et al. 2006; Yadav et al. 2010), the Arctic Oscillation/North Atlantic Oscillation (Gong et al. 2001; Wu and Wang 2002a, b, Yadav et al. 2009; Syed et al. 2010; Filippi et al. 2014), and the Polar Eurasia Pattern (Lang and Barros 2004). However, linkages between global modes of variability and upper-level geopotential height are complicated by competing influences between modes (Hoell and Funk 2013; Cannon et al. 2014) as well as documented feedbacks (Cohen et al. 2007). Additionally, there is not a linear relationship between the dynamics associated with the intensity of a disturbance and the amount of precipitation received in HMA (Lang and Barros 2004). Factors including the location of the WWD track, the depth of the trough, the duration of the disturbance, and moisture sources are all of necessary consideration.

Extratropical cyclones, including WWD, are fundamental features of the atmosphere that redistribute energy, momentum, and moisture at global scales while intimately linking large-scale circulation to regional-scale processes (Carlson 1998; Neu et al. 2013). Within HMA, there is no mechanism that is more important in contributing to water supply during winter, and therefore, it is important that we create a baseline climatology of WWD and further explore variability over time. Eulerian methods of investigating variance of fields related to WWD at synoptic scales are typically employed as a general measure of storm track activity (Lang and Barros 2004; Barlow et al. 2005; Syed et al. 2006; Yadav et al. 2010; Cannon et al. 2014). However, Eulerian statistics cannot convey important information regarding the specifics of individual systems, nor can the attributes of a cyclone be taken directly (Hoskins and Hodges 2002). Thus, a Lagrangian method of automatically tracking WWD, which can provide complementary information about individual systems and allows us to investigate track activity, is desired (Syed et al. 2010).

Over recent decades, many diagnostic methods of objectively identifying extratropical cyclones have been developed (Murray and Simmonds 1991; Hodges 1995; Serreze 1995; Blender et al. 1997; Sinclair 1994; Simmonds et al. 1999; Lionello et al. 2002; Benestad and Chen 2006; Trigo 2006; Wernli and Schwierz 2006; Akperov et al. 2007; Rudeva and Gulev 2007; Inatsu 2009; Kew et al. 2010; Hewson and Titley 2010; Hanley and Caballero 2012). Depending on the definition of a cyclone, these automated algorithms utilize differing variables and tracking techniques (Hoskins and Hodges 2002). Syed et al. (2010) first employed the tracking algorithm of Murray and Simmonds (1991), further refined by Simmonds and Keay (2000), to investigate WWD behavior in relation to teleconnections. This study heralded the benefits of Lagrangian tracking in HMA, and here, we demonstrate a simplified, easily reproducible methodology to track WWD, which often propagate along relatively low latitudes, encounter highly variable topography, exhibit strong tropical influences, and are highly asymmetric. Chen and Bromwich (1999) noted the difficulties of synoptic analysis in mountainous regions, the most complex of which is HMA on account of its vertical and horizontal extent, thus greatly reducing the number of observable pressure levels over a large area. Here, we propose a new tracking procedure for synoptic-scale disturbances based on the signature of WWD in 500-hPa geopotential height. A 500-hPa geopotential height is often employed to investigate the behavior of Rossby waves in subtropical and extratropical latitudes (Carlson 1998) and is thus a commonly used variable in HMA wintertime climate studies (Subbramayya and Raju 1982; Lang and Barros 2004; Hatwar et al. 2005; Syed et al. 2010).

The primary objective of this work is to investigate changes in WWD behavior with respect to HMA precipitation during

winter seasons from 1979 to 2013. In this study, we utilize negative 500-hPa geopotential height anomalies to identify individual WWD responsible for KH precipitation and track their progression. Our novel WWD tracking methodology, explicitly created to improve identification over high topography relative to other mid-latitude disturbance tracking procedures, provides an inventory of location, timing, intensity, and duration of events, which are explored in depth with an emphasis on seasonal variability. This provides a valuable link between the large-scale climate, transient disturbances, and hydrologic processes within the KH and allows us to evaluate WWD on a per-case basis while considering all factors that relate these systems to precipitation in the mountains. These factors include the intensity of systems as defined by the depth of 500-hPa anomalies at their center, wind speed intersecting topography, and precipitable water throughout the winter season. Furthermore, how WWD characteristics evolve over the course of a season in response to changes in the background climate is investigated, with the goal of understanding dynamic and thermodynamic influences on the relationship between these events and KH precipitation. Strong orographic forcing is known to reduce the efficiency of topography in converting advected moisture to precipitation, whereas convective events do not typically propagate as far into the orogenic interior (Bookhagen and Burbank 2010; Wulf et al. 2010).

The manuscript is organized as follows. Section 2 introduces the data. Section 3 explains the tracking methodology and is followed by Section 4, which validates the method's performance. Section 5 discusses the frequency of disturbances. Section 6 compares two sources of precipitation data during identified WWD events and Section 7 investigates the dynamics of these events. Section 8 concludes our manuscript.

2 Data

Meteorological data within topographically heterogeneous HMA is limited. In HMA, the observation network thins considerably due to increased elevation and remoteness. Furthermore, extant data is generally of poor quality due to sampling errors or biases. This research utilizes remotely sensed satellite precipitation estimates and reanalyses as the best available options for gridded meteorological data over recent decades.

Precipitation from the Tropical Rainfall Measurement Mission 3B42V7 (TRMM) (Huffman et al. 2007) and Climate Forecast System Reanalysis (CFSR), from the National Centers for Environmental Prediction (Saha et al. 2010), are used to identify heavy precipitation events in HMA. TRMM provides 3-hourly precipitation estimates at near-global 0.25° horizontal resolution for the period 1998–2013. The product combines TRMM 2B31, TRMM 2A12, special sensor microwave imager, advanced microwave scanning radiometer, advanced microwave sounding unit, and Climate Prediction Center infrared observations to estimate precipitation over low/mid-latitudes and is calibrated by station data. TRMM has documented deficiencies in capturing snowfall, which are especially problematic in HMA during winter (Lang and Barros 2004; Barros et al. 2006; Maussion et al. 2014). Because accurately quantifying total precipitation accumulation is difficult, our focus is on the timing and the relative precipitation contribution of WWD events, compared to all other dates. Under the assumption that low-elevation rainfall within the mountains is typically concomitant with high-elevation solid-state precipitation during WWD events, we can identify the dates of heavy precipitation events relative to all other dates by examining TRMM data. A similar procedure was performed in Cannon et al. (2014). We note that it is unlikely that the magnitude of precipitation in TRMM is accurate and that the proportion of high-elevation solid-state precipitation to low-elevation rainfall is not constant (Lang and Barros 2004).

Daily CFSR precipitation is also used to identify the timing of heavy precipitation events with an extended temporal record. CFSR is available at 0.5° horizontal resolution for the period 1979–2013. CFSR was chosen on account of its model coupling, spatial resolution, and modern assimilation system (Saha et al. 2010). For both TRMM and CFSR, we have aggregated to daily precipitation totals. Within the manuscript, we compare TRMM and CFSR during WWD events as independent indications of precipitation. Daily CFSR is also used to investigate the dynamics of WWD. Analysis of geopotential height, wind, moisture, and temperature is performed at near-surface and 500-hPa levels. Both the total fields and anomalies are considered, with the anomalies being derived by removing the mean seasonal cycle 1979–2013.

3 Tracking method

Extratropical cyclones, including WWD, have a characteristic depression in the 500-hPa geopotential height field, which differentiates these systems from the background flow and facilitates detection. The approach of our WWD tracking methodology is to apply the spatial correlation of standardized 500-hPa geopotential height anomaly features to track synoptic trough trajectories associated with extratropical cyclones. Similar methods have been used to track mesoscale convective systems based on cloud-top temperatures (Carvalho and Jones 2001) and large-scale convective features based on outgoing longwave radiation (Carvalho et al. 2002; Jones et al. 2004). Standardization of the 500-hPa geopotential height

input field by monthly mean variance accounts for increased variability in geopotential height with increasing latitude and allows for the identification of events based on the relative departure from normal. Standardized geopotential height has previously been used to investigate trough depth relative to typical conditions (Grumm and Hart 2001). Our procedure facilitates the detection of WWD in subtropical latitudes and in regions of high topography. Figure 1 exemplifies the tracking procedure and is used in the following paragraph as a visual aid to understanding the general principles on which our methodology is built. This is followed by a detailed discussion of the steps that comprise our algorithm.

Figure 1a, b shows the relationship between 500-hPa geopotential height anomalies (black contours) and standardized geopotential height anomalies (white dashed contours) for two WWD events affecting HMA. Figure 1a shows a characteristic mid-winter WWD occurring on February 18, 2003 and exhibiting a well-defined trough in 500-hPa anomalies, while the late season March 2006 event in Fig. 1b exhibits a comparatively shallow 500-hPa anomaly. The use of standardized anomalies augments the signal of the features relative to the background flow and has enabled the tracking of both troughs, each of which represents a significant deviation from local average conditions. These WWD produced 95th percentile precipitation (based on independent events in CFSR climatology) in the Karakoram (Fig. 1a) and central Himalaya (Fig. 1b). The large red dot indicates the position of the track center for the current day, and the smaller red dots, connected by a red line, indicate the position of the disturbance's center on preceding days, beginning with the first day of identification. The synoptic conditions that produced the events observed in Fig. 1, with respect to the benefits of our tracking method in identifying them, are discussed

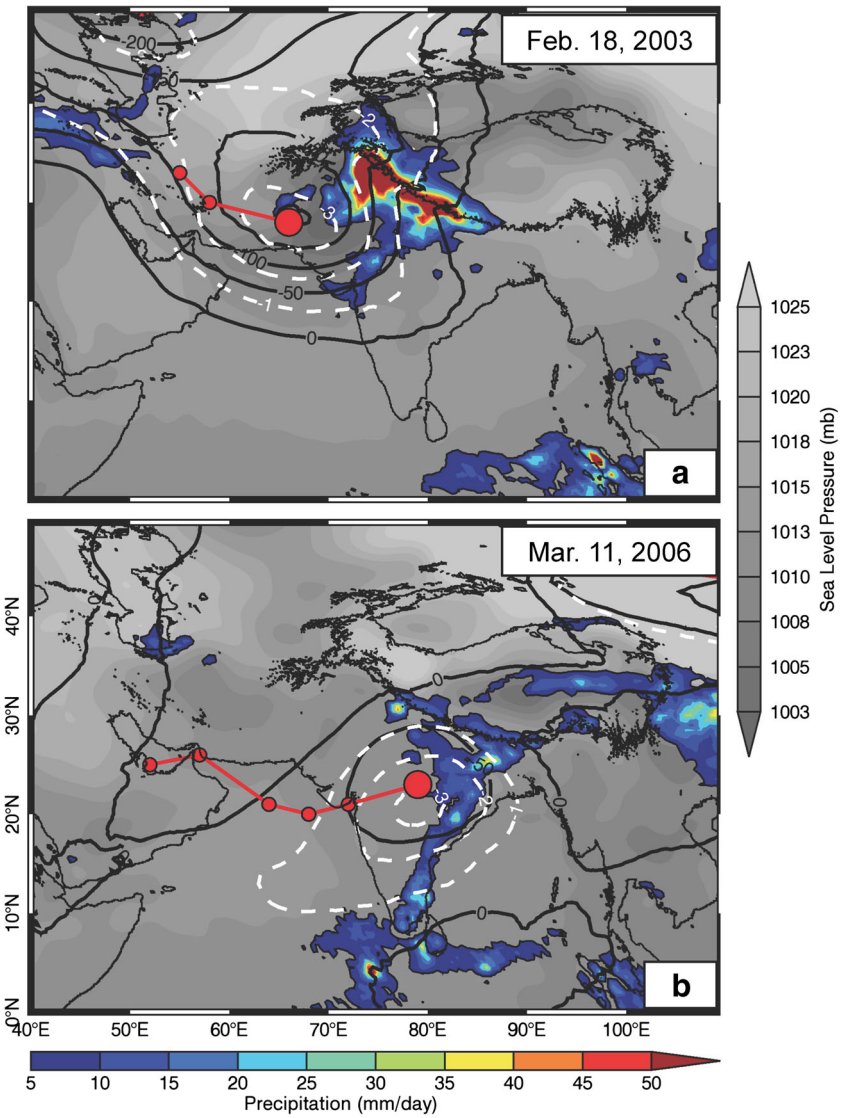

Fig. 1 **a**, **b** Example of 500-hPa wave-tracking methodology for two westerly disturbances. *Black contour* indicates 500-hPa geopotential height anomaly (m). *White dashed contour* indicates standardized 500-hPa geopotential height anomaly (interval is −1 standard deviations). *Red line* indicates disturbance trajectory. *Red dots* indicate location of center of disturbance on previous days. *Large red dot* indicates location of disturbance on current day. Sea level pressure (*gray*) and precipitation (*color*) shading apply only to current day

in Section 4. Our tracking methodology is detailed as follows.

1. Input data is CFSR 500-hPa geopotential height, aggregated to 1° horizontal resolution over the Northern Hemisphere. We consider daily maps of standardized 500-hPa geopotential height anomalies for the time period 1979–2013. For each daily map, we apply a series of standard deviation thresholds to retain only data exceeding the given threshold of standardized geopotential height anomaly. Our threshold procedure begins at −5 standard deviations and is incrementally relaxed by 0.25 per step toward −1 standard deviation. For each applied threshold, all data points not satisfying the threshold are set to null value to create a background mask. The more restrictive the threshold, the smaller the area of geopotential height anomalies retained. Using maps of decreasing restrictiveness allows us to identify multiple centers within a single, large region of negative anomalies. For example, imagine a perturbation (wavenumber one or two) covering the majority of continental Asia, which propagates eastward very slowly relative to two or three embedded shortwaves that propagate eastward at a faster rate. In this scenario, incrementally relaxing our thresholds allows for the identification of the centers of each individual disturbance, whereas using only a single threshold would likely have resulted in a single track, exhibiting unrealistic behavior as it skipped between shortwaves embedded within the longwave.
2. After we have identified disturbances in geopotential height for a given threshold, we filter out apparently small features by removing identified regions comprised of fewer than 5 pixels across (5 pixels, or 5° is roughly 450 km at 35° N; the approximate latitude of the Karakoram). These features are common in the tropics where slight perturbations appear significant. This filtering, henceforth termed "the area threshold," ensures the presence of a spatially coherent mid-latitude disturbance. Also, it is worth noting that global CFSR 500-hPa data at 1° resolution intersects topography in only one grid point. Though this grid point is in our study area (containing K2 and the Gasherbrum Massif) and below the surface for roughly 17 % of the year, it does not disrupt the general circulation and we do not address this minor issue in our application of the dataset.
3. At this point, we retain two datasets: daily maps of the location and spatial extent of anomalies surpassing the first standard deviation threshold, in which the identified area also exceeded the area threshold (to be referred to as "the max map"), and daily maps of the location and spatial extent of anomalies surpassing the least restrictive (−1) standard deviation threshold, in which the area threshold was also exceeded. We locate the center of disturbances by first selecting all nonnull value regions in the max map and then identifying the spatially weighted center of the actual geopotential height anomalies within the active regions.
4. To track disturbances over time, we begin by calculating the spatial correlation of identified regions in the −1 standard deviation map between consecutive days. If the spatial correlation between two regions exceeds 0.3, we determine the disturbance at time $t+1$ to be a continuation of the disturbance at time t. The spatial correlation threshold of 0.3 was reached empirically in the initial development of the algorithm. We use the −1 standard deviation map rather than the max map to determine spatiotemporal correlation because the deepest regions of anomalies are typically disjointed at high standard deviation levels.
5. Once the algorithm has identified regions of negative geopotential height anomalies that are connected in time, the trajectory of the trough is created by linking corresponding centers between consecutive days. If, within an identified region in the −1 standard deviation map of time t, which is spatially correlated with a region on the subsequent day, there exists only one identified center, the track will begin at time t at that location. If the spatially correlated region on the subsequent day also contains only one identified center, the disturbance's track will be created by linking corresponding centers at times t and $t+1$. If multiple centers exist within a region, multiple tracks will be created. Given multiple centers in either time t or $t+1$, tracks are created by linking centers that are in closer spatial proximity. If the number of centers within a region passing the −1 standard deviation threshold changes between time t and time $t+1$, a merging or splitting of tracks has occurred. For splitting, an independent track is created at $t+1$ for the center furthest from the original track. For merges, the track with the longest duration to date is retained. This procedure is performed for each consecutive day of the dataset while retaining all track information from the previous day. If an identified center is not related to a preexisting track, a new one is created. Similarly, if an existing track cannot be linked to a spatially correlated region on the subsequent day, the track ceases.
6. Daily temporal resolution allows for centers of synoptic systems to propagate large distances between images. To create continuous tracks, track centers for consecutive days were linked using the shortest straight line distance interpolation to connect adjacent grid points between centers. The final product of our tracking procedure is daily-resolution 500-hPa trough tracks over the northern hemisphere for the time period 1979–2013.

4 Tracking verification

In the previous section, we detailed the methods by which we identify and track 500-hPa troughs. Here, we examine two troughs that produced large precipitation totals in the Himalaya to elucidate how the tracking method works in practice. The February 2003 event, shown in Fig. 1a, is characterized by a deep upper-level trough, exhibiting negative 500-hPa geopotential height anomalies in excess of 200 m at the center. With respect to the climatology of WWD, this represents a strong, but archetypical event. This event developed 2 days prior, from an existing trough over the Caspian Sea. The March 2006 event (Fig. 1b) was caused by the interaction of a WWD, exhibiting a shallow upper-level trough (between −50 and −100 m on March 11th), with a moist tropical air mass over the Indian subcontinent. The track, observed over the Arabian Sea and India, originated on the 6th of March as a shortwave at approximately 50° E, 25° N and propagated zonally toward the central Himalaya. By the 11th (Fig. 1), the trough was positioned over central India and the resultant southerly moisture transport driven against the Himalaya was sufficient to produce an extreme precipitation event (Norris et al. 2014).

Neither event displayed changes in sea level pressure that were remarkable or exclusive to extratropical cyclones, precluding their identification in many of the tracking algorithms discussed by Neu et al. (2013), which rely on well-structured features at lower levels. The general dissociation between premonsoon storms in this region and lower-tropospheric circulation was first observed by Ramaswamy (1956), in which the usefulness of upper-tropospheric charts for forecasting these events was also discussed. Furthermore, any methodology employing data below the 500-hPa level would be significantly affected by high topography over much of central Asia and yield dubious results. It is also worth mentioning that a number of tracking algorithms, including that of Murray and Simmonds (1991) and Hodges (1995), which were originally designed to identify surface systems, can be modified to incorporate middle tropospheric variables, such as done by Keable et al. (2002), Hoskins and Hodges (2002), and Syed et al. (2010).

For both events, the standardized negative 500-hPa geopotential height anomalies were 3 to 4 standard deviations below normal, thus facilitating the tracking of WWD using our methodology. This example of events occurring in different locations, during different times of the year, with varying trough depth was specifically chosen to demonstrate that the tracking methodology performs well irrespective of track latitude, intensity, or timing. However, we note that not all systems are as well behaved, and there are rare instances where the methodology has difficulties: notably, when stationary waves covering expanses of central Asia linger for many days with periodic extensions of their troughs toward HMA or when multiple tracks are recorded in close proximity over several days. Uncommon cases such as these are observed to produce unrealistic tracks.

Figure 2 shows a global 500-hPa wave track density map for the Northern Hemisphere winter (November–April) for the time period 1979–2013. Density is defined as the total number of tracks recorded in a given grid point through time, with minimum distance interpolation performed between consecutive day's centers. Over southwest and central Asia, the region of WWD activity, an appreciable maximum in track activity exists. This region of increased activity is colocated with the subtropical jet, which may act as a baroclinic waveguide (Krishnamurti 1961; Hoskins and Ambrizzi 1993; Ridley et al. 2013). Enhanced activity is also identifiable in the North Pacific, across the USA, and over the North Atlantic, colocated with the mean position of the maximum zonal wind in the mid-troposphere during winter. We note that as a result of using standardized 500-hPa anomalies, the regions of maximum track density appear to be shifted equatorwards compared to the results from many other tracking methods, which employ low-troposphere variables. This work focuses on the propagation of troughs as identified by perturbations in 500-hPa geopotential height, which shows a characteristic response to WWD, and not on replicating storm tracks as identified by other methods as reviewed by Neu et al. (2013). However, our maps of track density strongly resemble those of Hoskins and Hodges (2002), in which several variables at upper levels were used to investigate winter storm tracks. Notably, both our method and the established Hoskins and Hodges method as well as the analysis performed by Syed et al. (2010) identified a maximum in track density in the vicinity of the mid-latitude jet, where WWD develop.

To demonstrate the relationship between disturbances identified by our method and precipitation, an index of extreme precipitation events was created for the western Himalaya/Karakoram (74–78° E, 34–37° N) (KH) by spatially averaging CFSR daily precipitation estimates for the region and retaining the 95th percentile of independent (3 days between events) nonzero precipitation dates during winter (NDJFMA). Figure 3 displays the density of all tracks that recorded a segment concomitant with an extreme precipitation event. The 500-hPa geopotential height anomaly is also composited onto the index of extreme precipitation. A depression is observed centered several degrees to the west of the KH as demonstrated in Cannon et al. (2014). Track density in this figure indicates that extreme precipitation in the KH is associated with the propagation of WWD across southwest/central Asia between 25° N and 35° N.

Our WWD tracking method is proven to accurately identify the primary atmospheric circulation pattern that produces KH precipitation events. Heavy precipitation events are particularly well represented, as these are characteristically associated with the systems we are tracking. We note that many of the lighter precipitation events are not related to characteristic WWD

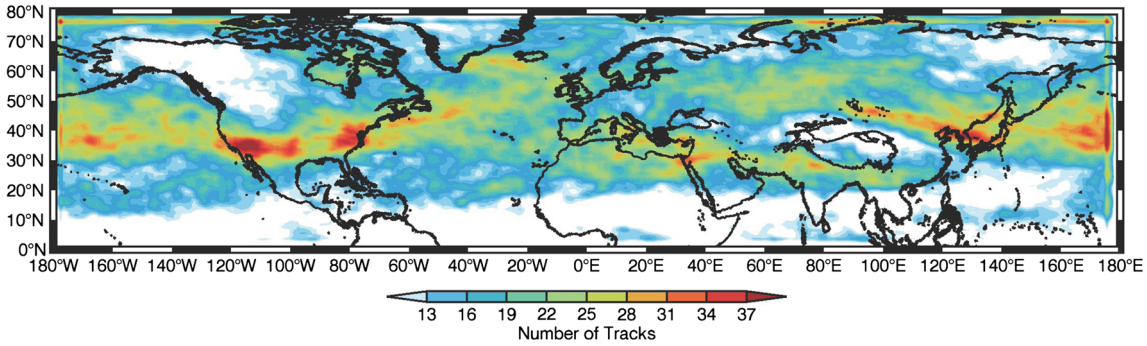

Fig. 2 Global 500-hPa wave track density map indicating trajectories of centers of disturbances recorded during winter seasons (November to April), 1979–2013; 3000 m elevation contour of the Tibetan Plateau is indicated as a *black line*

circulation and are not captured. Therefore, the average seasonal precipitation may not be accurately represented. Additionally, WWD in our region of interest do not always produce precipitation. These issues are further discussed in the subsequent sections along with the statistics of trough depth, cross-barrier wind speed, and precipitable water content of individual events.

5 Westerly disturbance properties

The average properties of WWD, including their intensity, size, duration, and associated precipitation, vary according to their location. The variability in latitude between disturbances alters their interaction with high mountain Asia by changing the angle of incidence between topography and circulation; thus, it is necessary to investigate WWD according to several subregions. We subdivided the greater region of WWD activity into three subregions of varying latitude to explore the effect of storm track location on system dynamics and resulting KH precipitation. Figure 4 shows the regions in which we investigated WWD events: the outer domain (50–80° E, 15–50° N), region 1 (60–75° E, 25–40° N), region 2 (60–75° E, 15–25° N), and region 3 (60–75° E, 40–50° N). Figure 5 indicates the number of track center trajectories intersecting each of the designated regions of WWD propagation (Fig. 4) per winter season. The outer domain is the general region in which troughs propagating through will have a high probability of influencing weather in the KH. Region 1 indicates the region of maximum activity within the outer domain. Troughs entering this region are most frequent (5–6 per year, Fig. 5b) and affect the KH most directly. This region is also colocated with the mean position of the subtropical jet over southwest Asia during winter (Cannon et al. 2014, their Fig. 11a). Regions 2 and 3 represent areas that also experience WWD, though their influence in the KH is less direct than region 1 and generally less frequent, exhibiting an average of approximately 2 per year per region (Fig. 5c, d).

The total number of recorded WWD as well as the number of region 1 WWD shows interannual variability for the period 1979–2013, but a statistically significant trend in the number of these events per season cannot be determined based on the short record. This is interesting because it indicates that the frequency of WWD in the region of maximum activity has not changed.

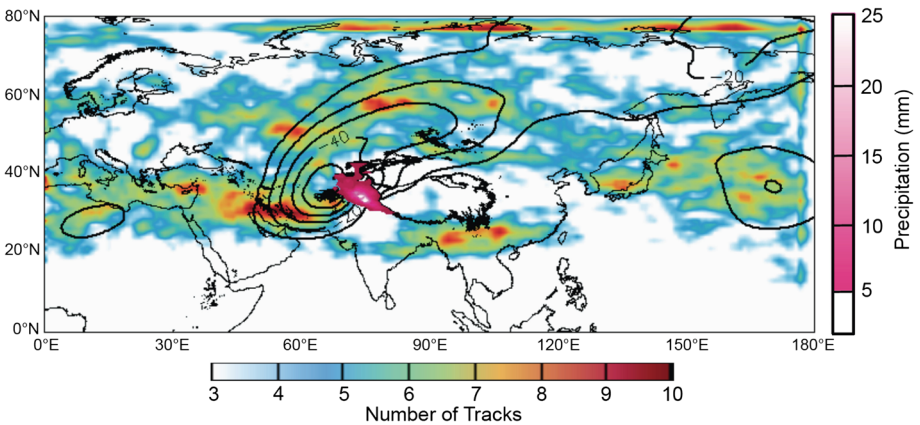

Fig. 3 A 500-hPa wave track density map indicating trajectories of centers of disturbances recorded during 95th percentile precipitation dates in the Karakoram (November to April), 1979–2013. *Black contours* indicate negative 500-hPa geopotential height anomalies (m). *Pink shade* over Karakoram indicates precipitation intensity; 3000 m elevation contour of the Tibetan Plateau is also shown as a *black line*

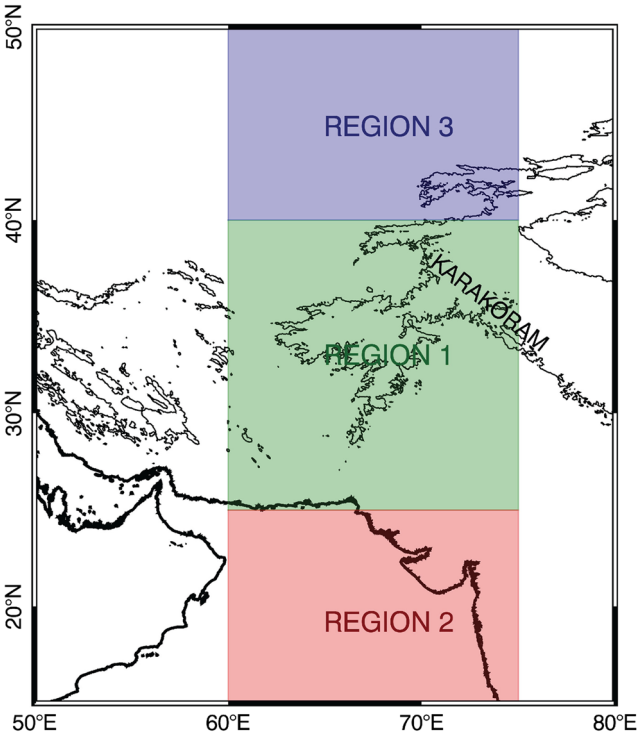

Fig. 4 Schematic map indicating regions used to index westerly disturbances. *Thin black line* indicates 3000 m elevation contour

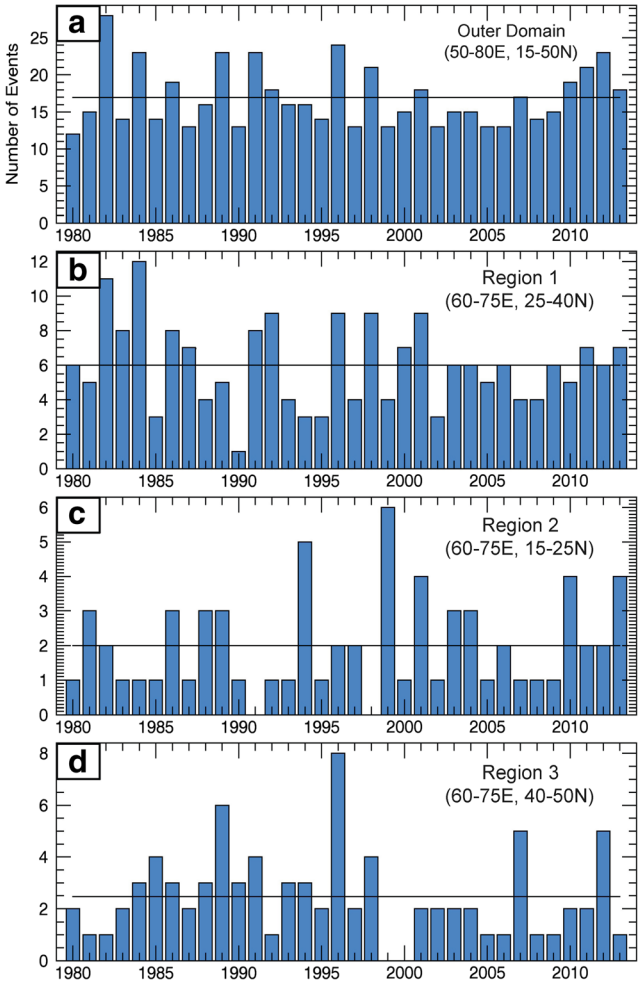

Fig. 5 **a**–**d** Number of wave track center trajectories intersecting each of the regions displayed in Fig. 4 per winter season. *Black line* indicates average number of disturbances in the given region per winter (November to April) 1979–2013. Note that the *Y*-axis is not constant between panels

With respect to the findings of Cannon et al. (2014), which indicated an increase in the synoptic variability in the upper-level geopotential height field for this region, this may signify an increase in the intensity rather than the frequency of WWD. It is also important to note that global modes of atmospheric variability, such as El Niño Southern Oscillation (ENSO), likely play a role in the distribution of events per region. Previous studies have indicated a significant barotropic Rossby wave response of upper-level geopotential height over southwest-central Asia to ENSO, resulting in intensified westerly jet activity and a deepened trough during El Niño (Syed et al. 2006; Yadav et al. 2010; Hoell et al. 2013; Cannon et al. 2014). Using our tracking methodology, we also observed a drastic increase in the number of WWD during El Niño events (not shown), as well as global influences of ENSO on geopotential height variability. The focus of this manuscript is on understanding the dynamics of WWD and their variability through time. For the remainder of this work, we concentrate on WWD tracks recorded in region 1 (60–75° E, 25–40° N), the region with the most events and strongest relationship with KH precipitation.

6 TRMM and CFSR comparison of WWD precipitation in the Karakoram and western Himalaya

Given the difficulties associated with estimating precipitation in mountainous regions using satellites (Barros et al. 2000; Anders et al. 2006; Bookhagen and Burbank 2006) and models, it is necessary to briefly compare the two precipitation products used in this study. In Section 2, we introduced some of the issues associated with CFSR and TRMM precipitation; here, we show the relationship between the two products during the maximum precipitation day of WWD in region 1 as indexed from CFSR data (Fig. 6). For this analysis, TRMM is interpolated to the 0.5° CFSR grid. Figure 6a indicates the Pearson product-moment correlation between CFSR and TRMM for the maximum precipitation day of each event affecting region 1 (2000–2013, 84 events). Correlation in the Karakoram and western Himalaya is between 0.5 and 0.8. Figure 6b is a regression of area-averaged TRMM and CFSR precipitation estimates for the Karakoram (74–77° E, 34–37° N) during those WWD. The red dots indicate events where CFSR was more than three times greater than the TRMM estimate. This was observed most frequently in low-precipitation events. On an accumulated monthly precipitation

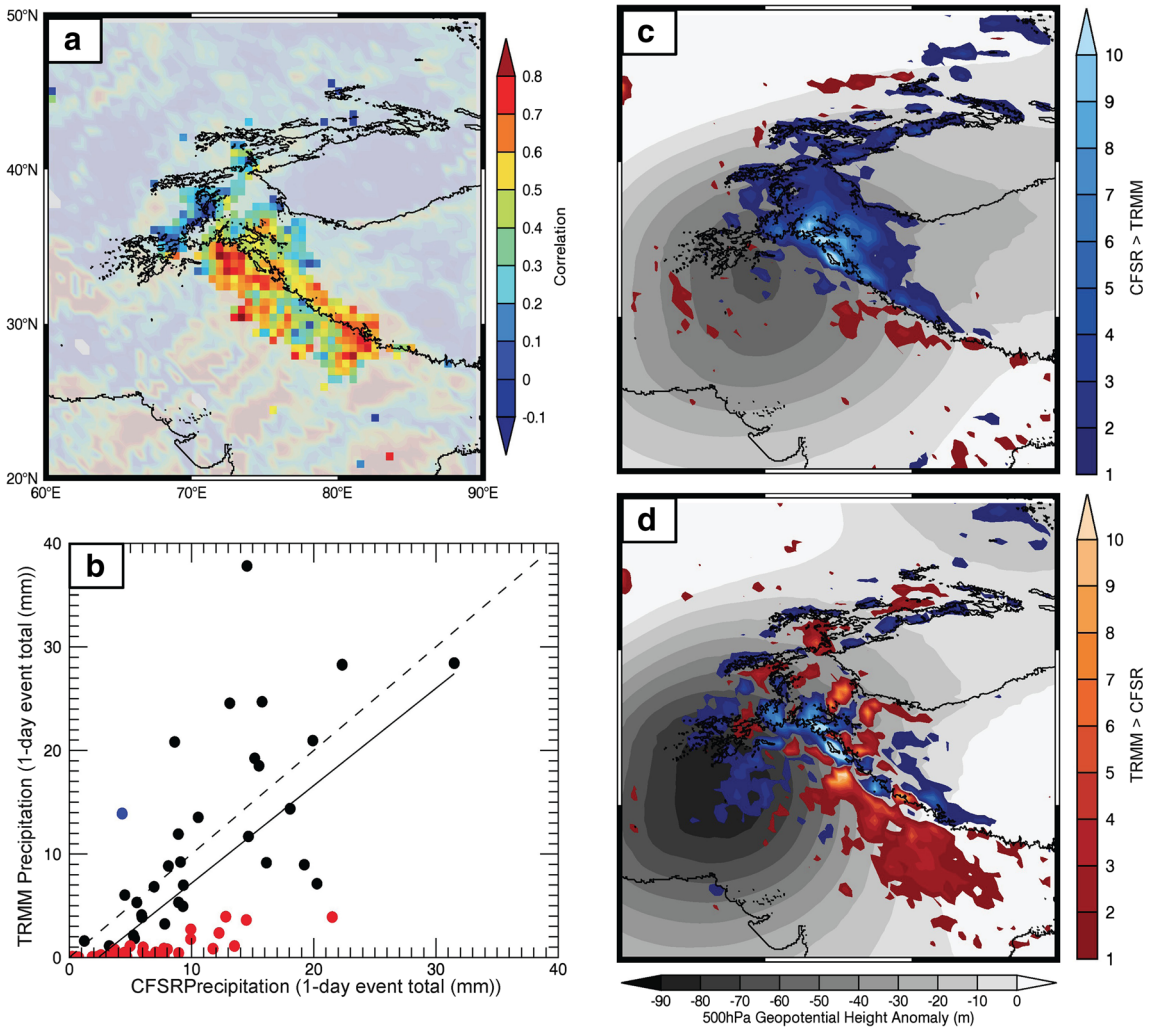

Fig. 6 Correlation between TRMM and CFSR precipitation delivered to Karakoram by region 1 westerly disturbances, 2000–2013 (**a**). The *faded regions* indicate that the observed precipitation was less than 1 mm. **b** Regression of 1-day precipitation totals delivered to Karakoram by region 1 westerly disturbances. *Red dot* indicates event where CFSR precipitation recorded was more than three times greater than TRMM precipitation. *Blue* indicates the opposite and *black* is in between. **c** A composite of precipitation differences between CFSR and TRMM and geopotential height anomalies for *red dot* events. *Black dot* events are composited in **d**. *Color bars* for **c** and **d** apply to both figures

basis, CFSR generally exceeds TRMM precipitation estimates during winter months in high mountain Asia (not shown). We do not evaluate how much of this difference is attributable to TRMM's difficulty in estimating light and solid-state precipitation and how much is based on CFSR overestimation, though previous work by Maussion et al. (2014), which evaluated TRMM, station gauge, reanalysis, and dynamically downscaled precipitation products to find that differences between products vary on account of season, location, and precipitation type, also identified issues in the ability of TRMM to properly represent high-elevation solid-state precipitation in regions of strong winter westerly disturbance influence.

A comparison of composites of 500-hPa geopotential height anomalies for WWD where CFSR precipitation estimates in the KH were more than three times greater than TRMM (Fig. 6c), compared to all other events (Fig. 6d), indicated that deeper troughs are associated with more similar precipitation estimates. Analysis of the centers of tracks for dates when CFSR was three times greater than TRMM (49 events) and dates when CFSR was less than three times greater than TRMM (35 events) indicated the mean depth of 500-hPa anomalies to be −96 m for events when CFSR greatly exceeded TRMM and −117.6 m for events when CFSR did not exceed TRMM by a factor of 3. A *t* test determined the difference in WWD depth to be significant at the 5 % confidence level. This is likely attributable to deep troughs producing comparatively heavy precipitation, which should be more accurately represented by both products as the signal is stronger and covers a greater area.

Figure 7 shows the mean TRMM and CFSR precipitation amount for the single maximum precipitation day of 84 events (2000–2013; indexed using CFSR) for the Karakoram region.

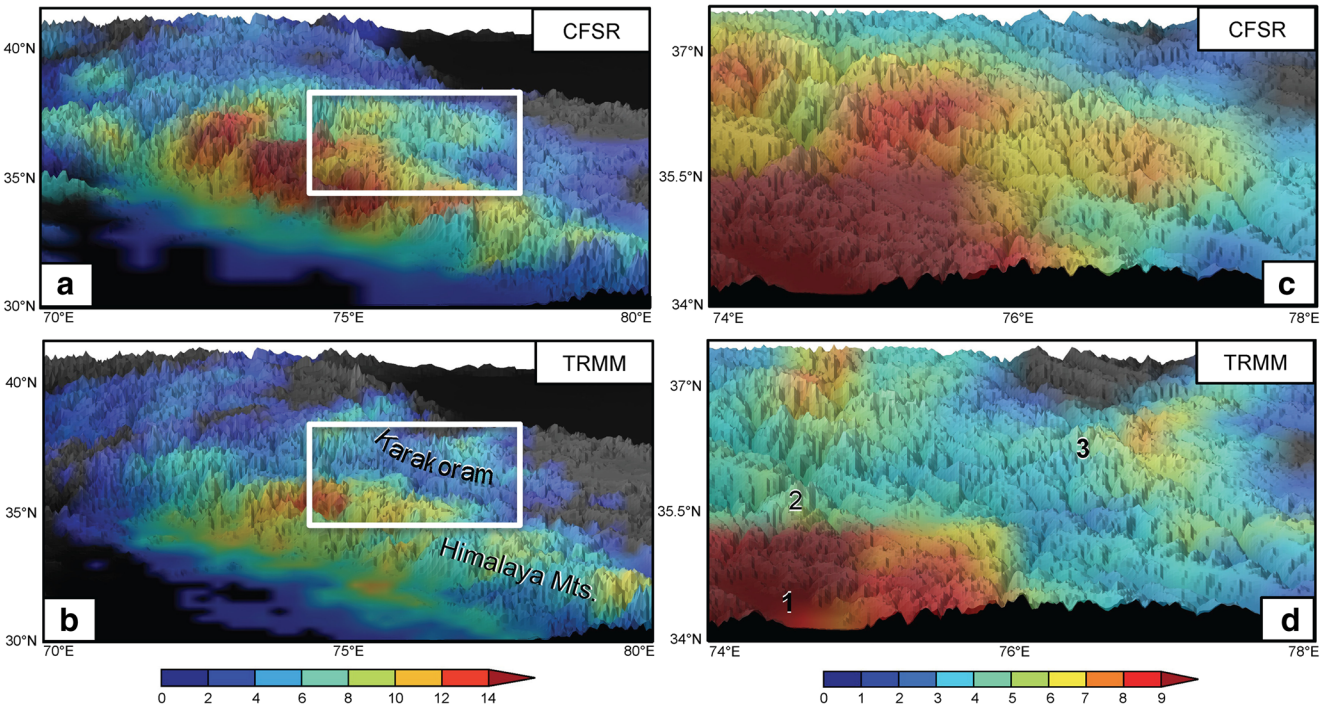

Fig. 7 Average Karakoram precipitation recorded during westerly disturbances in winter seasons when TRMM and CFSR data were available (1998–2013). Topography is shown in three dimensions. CFSR outer domain (**a**) and inner domain (**c**) and TRMM outer domain (**b**) and inner domain (**d**). *1* Location of Kashmir Valley. *2* Nanga Parbat. *3* K2. *White box* in **b** indicates domain for **c** and **d**

In both products, the maximum in precipitation is found on the southern (windward) slope of the western Himalaya, which protrudes abruptly from the Gangetic Plain. Additionally, there is consistency in indicating a secondary maximum in the Karakoram Mountains, which are further downwind, in the interior of the ranges. Though the spatial distribution is similar between CFSR and TRMM, it is again observed that CFSR has a higher mean value on both the primary and secondary peaks. For this work, we have confidence that the spatial and temporal distribution of precipitation during individual events is accurate, given the consistency between datasets. However, without dependable in situ measurements, we are doubtful that the magnitude of precipitation is reliable. We employ CFSR precipitation for the majority of this manuscript on account of its extended temporal record, though additional research (not shown here) has indicated similar results using TRMM (1998–2013).

7 Seasonal variability of WWD and precipitation contribution

Tracking individual westerly disturbances and investigating their collective statistics illuminates the manner in which the mechanisms that drive orographic precipitation during these events change throughout the winter season. WWD are primarily active from November through April and exhibit strong seasonal variability (Lang and Barros 2004). Additionally, general changes to the atmosphere due to the seasonal cycle create significant differences between individual disturbances according to when they occur in the winter season. Figures 8, 9, and 10 illustrate changes in WWD over the winter season as identified through our tracking approach. Figure 8 indicates the number of region 1 WWD recorded in each month for each year of CFSR (1979–2013). We observe a large interannual variability in the number of WWD with some years exhibiting three or more events per month and others no event. The March time series in Fig. 8 is the best illustration of the year-to-year differences in the number of disturbances. Moreover, the environmental conditions in which WWD develop vary throughout the winter season. To illustrate these differences, Fig. 9 shows composites of 500-hPa geopotential height anomalies, vertically integrated moisture transport, and precipitation, for WWD events, as indexed by wave tracking, in each month of the winter season. In December, January, and February, the average geopotential height anomaly is up to 70 m deeper than in March, April, or November. From December through February, the meridional temperature gradient across the northern hemisphere is at a maximum, and thus, mid-latitude storm intensity peaks during this time (Ramaswamy 1956). WWD occurring during these months are dynamically more intense, with deeper troughs and stronger wind speeds than those occurring in March and April. However, through the Clausius-Clapeyron

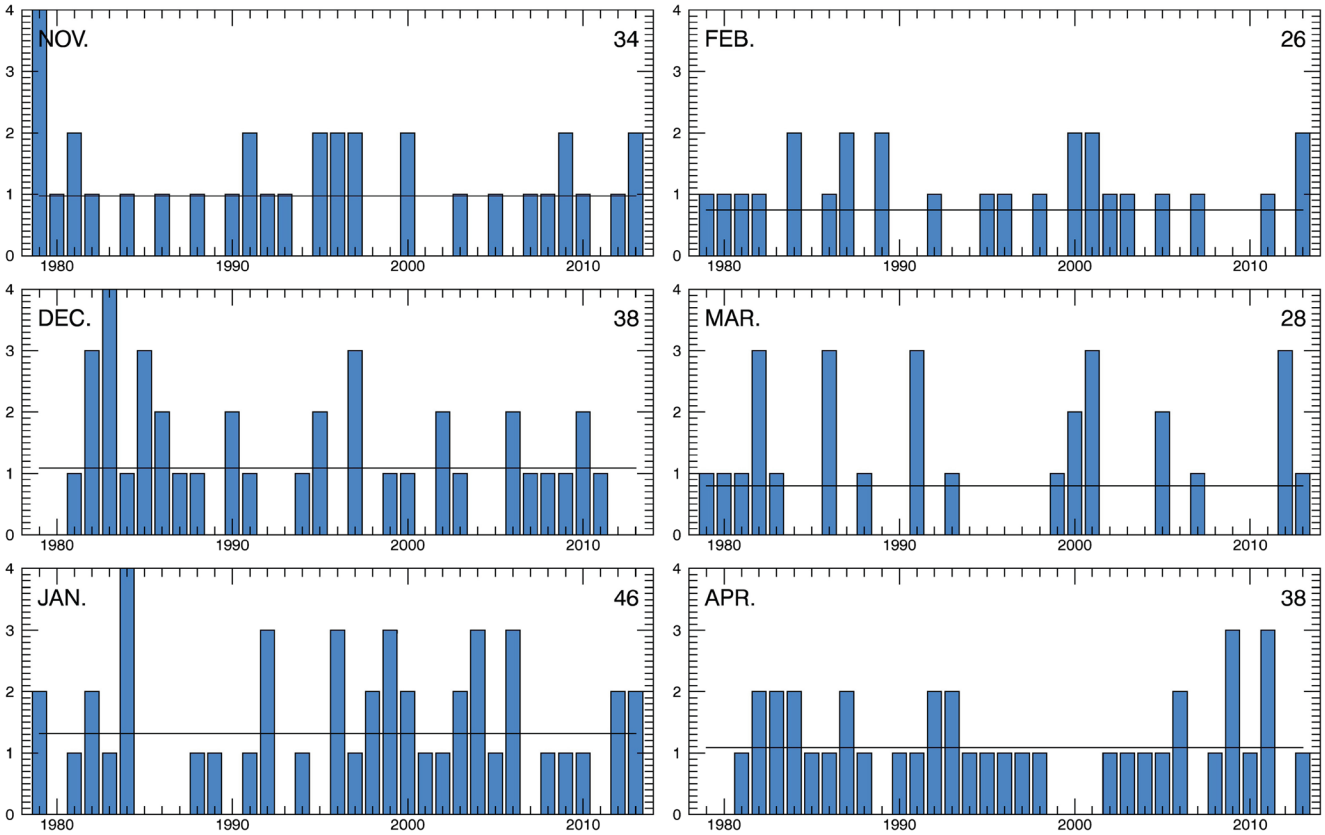

Fig. 8 Number of wave track center trajectories intersecting region 1 per month. *Black line* indicates average number of disturbances in the given region per month, 1979–2013. *Number in the upper right* indicates the total number of disturbances

relationship, elevated temperatures in spring increase moisture content, as evidenced by the high precipitable water values observed over continental areas in March and April (Fig. 10). This produces a less thermodynamically stable atmosphere, in which reduced dynamical forcing may still trigger orographic precipitation in the KH. Figure 10 shows increased precipitable water along the Himalayan Arc in spring months relative to mid-winter months as well as weaker 500-hPa meridional wind speed for late season WWD. March is the most variable month as WWD transition from primarily orographic to orographic and convective forcing. After April and before the onset of the monsoon, large-scale convection is unlikely as the subtropical jet has migrated to the north of the Tibetan Plateau and upper-level divergence associated with waves in the jet is absent (Ramaswamy 1956).

Heavy precipitation events associated with WWD can occur in any month during the winter season, but are driven by different processes according to their timing. As noted, the upper-level trough is, on average, deeper from December through February and associated meridional wind velocities are stronger than in March and April, thus impinging on the KH with more intense orographic forcing. Figure 9 indicates little change in vertically integrated moisture flux (vectors) between these months, though the dominant term appears to change from wind speed to precipitable water. Curio et al. (2015) discuss the mechanisms by which moisture is transported to the Tibetan Plateau and demonstrate that, in winter months, westerly disturbances are the dominant source of moisture, while in warmer months, the western Tibetan Plateau receives monsoon moisture in addition to advection from westerlies, while also benefiting from enhanced local evaporation, leading to moisture recycling.

In March and April, atmospheric moisture content is seen to increase due to rising temperatures, which increase saturation vapor pressure. Amplified moisture and temperature at low levels are a primary condition for convective instability, as measured by moist static energy change with height (not shown), during these events. In this premonsoon environment, the interaction of an extratropical cyclone with a relatively warm, moisture-laden, tropical air mass provides strong moisture transport toward the mountains. Figure 10 shows average precipitable water during April WWD events to be 25 % higher over the Gangetic Plain than during January events, while 500-hPa southerly winds are generally 2 m s^{-1} slower. Heavy precipitation in the Himalaya via orographic lifting experiences stronger contribution from thermodynamic instability, as the atmosphere is less stable than in the middle of winter (Norris et al. 2014). It is worth noting that Simmons

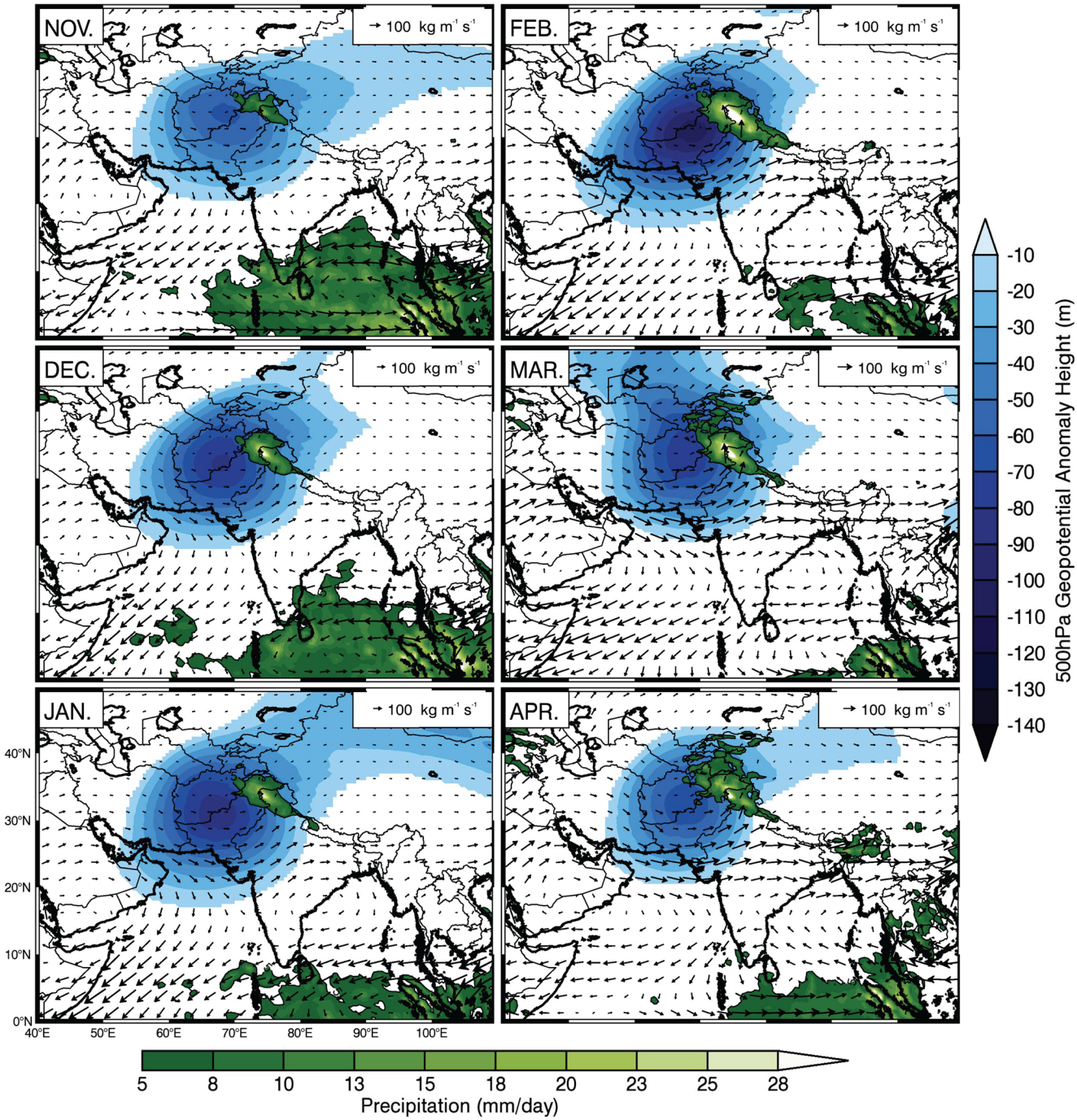

Fig. 9 Composites of westerly disturbance events as identified by the maximum Karakoram precipitation (CFSR) day of track trajectories intersecting region 1. Vectors indicate vertically integrated moisture flux

et al. (2010) show that surface temperature and humidity trends from two reanalysis products are in excellent agreement with estimates from climatological land data, and the work of Lu et al. (2014) and Curio et al. (2015) further supports the ability of reanalyses to represent in situ moisture conditions at coarse spatiotemporal resolution over the Tibetan Plateau. At finer spatial and temporal scales, reanalyses may be less representative of moisture conditions given their inability to resolve individual mountain valleys (Curio et al. 2015), which serve as moisture conduits (Bookhagen and Burbank 2010), but this is of minor importance with respect to our study given the magnitude of differences between seasons relative to the magnitude of differences in moisture advection resulting from the smoothing of local valley systems.

To further investigate the dynamics of WWD as well as the mechanisms that drive precipitation in the KH and to

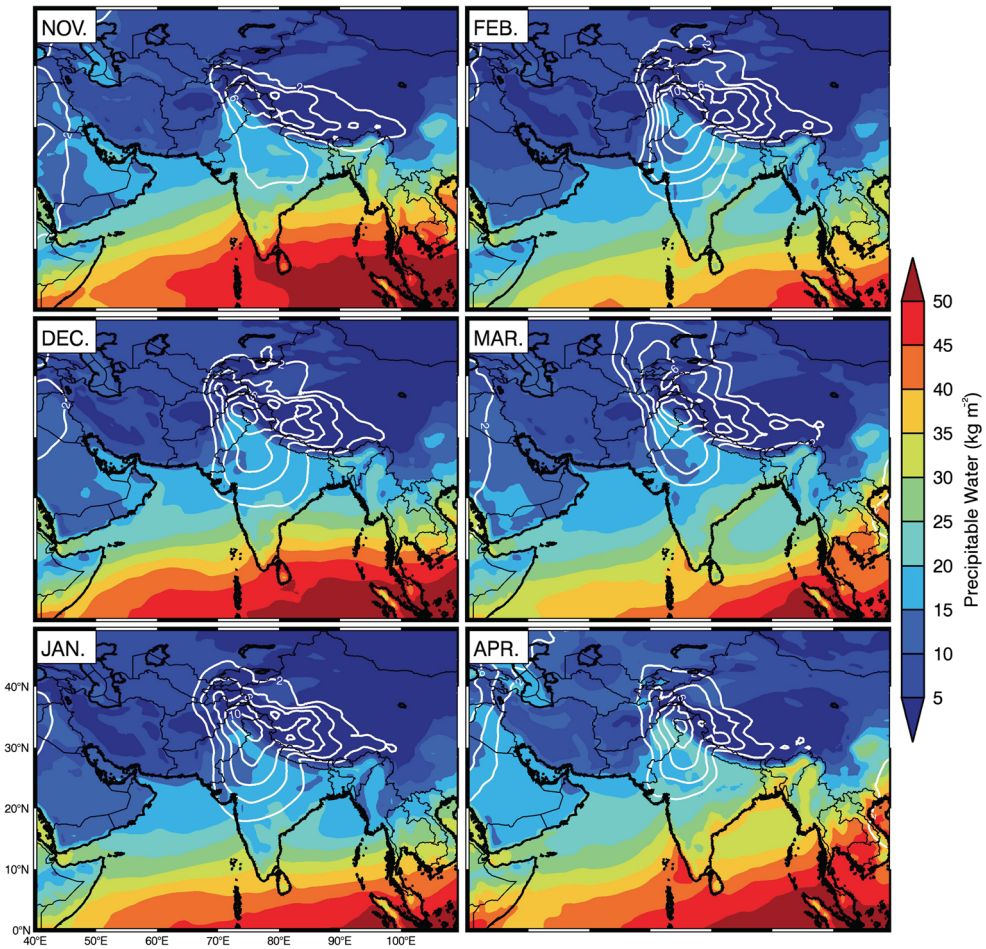

Fig. 10 Composites of westerly disturbance events as identified by the maximum Karakoram precipitation day (CFSR) of track trajectories intersecting region 1. *White contour* indicates the southerly 500-hPa wind speed (m s^{-1})

substantiate the argument proposed to explain Fig. 9, we performed a series of regressions between 500-hPa geopotential height anomalies at track centers, 500-hPa meridional wind in the KH (74–77° E, 34–37° N), total precipitable water in the KH, and precipitation in the KH (Fig. 11). Because the Karakoram is east-west oriented, meridional wind is perpendicular to the mountains and is the more important horizontal component of wind for orographic precipitation. These four variables have a complex relationship that defines winter weather in HMA. Additionally, moving away from composite analysis enables the identification of changes in the relative contribution of each variable to precipitation on a case-by-case basis. Though these figures delineate statistically significant patterns, they also demonstrate that the average values shown in the monthly WWD composites (Figs. 9 and 10) are derived from strongly varying individual events.

Correlation between WWD depth and 500-hPa meridional wind speed in the KH is 0.46 for 209 independent region 1 events occurring November through April 1979–2013 (Fig. 11a). Figure 11a also demonstrates differences in trough depth according to month as previously illustrated in Fig. 9. In December, January, and February, WWD are at maximum intensity as the mid-latitude jet is at its peak; the average depth of geopotential height anomalies is −115 m compared to −94 m for March and April events. Consequently, wind speeds in the KH (maximum value 2 days before precipitation maximum through 2 days after, for the region 74–78° E, 34–37° N) also peak during events falling in these months. Figure 11b shows a regression between 500-hPa meridional wind in the KH and precipitation. The correlation is 0.59, which is statistically significant at the 5 % level (p value for two-sided t test less than 0.05), indicating a positive relationship between the strength of the wind encountering topography and the amount of precipitation received, with high wind speeds enhancing precipitation over topography (Roe 2005). Coincident with increasing trough depth, wind speeds are highest in December, January, and February, leading to the conclusion that the orographic forcing of precipitation associated with WWD is at a maximum during these months. Interestingly though, precipitation accumulation is not necessarily highest at the same time, due largely to changes in available moisture.

Heavy precipitation events occurring in March and April have characteristically slower meridional wind speeds at upper levels (the average for 66 March and April events is 9.4 compared to 10.5 m s^{-1} for 110 events occurring December

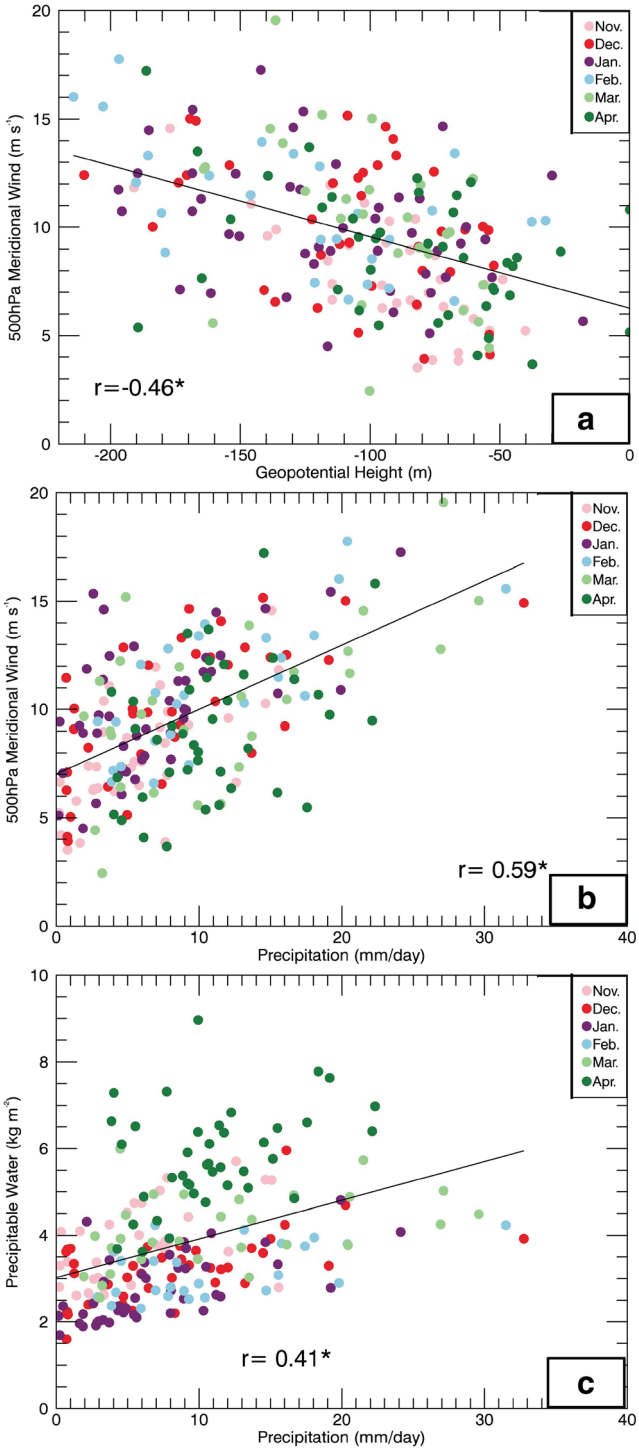

Fig. 11 Regression of variables during all region 1 westerly disturbances; 500-hPa geopotential height anomalies at the trough center and 500-hPa meridional wind in the Karakoram (**a**); 500-hPa meridional wind and precipitation in the Karakoram (**b**); precipitable water and precipitation in the Karakoram (**c**). *Dot color* indicates month (see legend). *Black line* indicates slope of regression. *Number* on the graph indicates Pearson correlation coefficient. *Star* next to the number indicates significance at 5 % confidence interval

through February), though the decrease in orographic forcing is compensated for by enhanced precipitable water, as noted earlier (5 compared to 3 kg m^{-2} for December through February events). Figure 11c indicates highest precipitable water in the KH to have occurred primarily during March and April WWD. Increased convective instability, slower storm propagation, and increased moisture all contribute to heavy precipitation despite reduced wind speed compared to middle of winter events.

Figure 12 delineates the relationship between precipitable water, 500-hPa meridional wind, and precipitation during region 1 WWD for December through February (Fig. 12a; 110 events) compared to March and April (Fig. 12b; 66 events). November is omitted in this analysis, as precipitation during this month is minimal. The intensification of negative geopotential height anomalies is associated with a strengthening of the pressure gradient, which yields southerly wind along the eastern edge of the disturbance and draws moisture from the Arabian Sea toward HMA. This can be observed in Fig. 12a by the significant positive correlation (0.35) between 500-hPa meridional wind and precipitable water. Additionally, the largest precipitation totals (greater than 24 mm/day) are recorded during strong wind and high precipitable water events. The well-balanced relationship deteriorates in March and April, when precipitable water is enhanced irrespective of the disturbance (Fig. 12b; r=−0.01). This is further illustrated by multiple regression analysis using precipitable water and 500-hPa wind as estimators of precipitation during past events, which yields an R^2 value of 0.56 for the December through February events, but only 0.31 for March and April.

Table 1 is introduced to summarize the results shown in Figs. 11 and 12 and to characterize the combined relationships among the investigated variables, which are not entirely independent. This table lists correlation values between all variables for December through February and March through April events. In agreement with Fig. 12, both 500-hPa meridional wind and precipitable water are better correlated to precipitation in mid-winter than early spring, and they are not independent at this time (r=0.35). The considerable weakening of the relationship between precipitable water and precipitation, from r=0.57 in mid-winter to 0.28 in spring, and precipitable water and meridional wind, from r=0.35 to 0.02, apparently results from a reduction in the dependency on WWD to provide sufficient moisture for precipitation, on account of the higher moisture content in the atmosphere irrespective of WWD occurrence. The relatively minor reduction in the correlation between 500-hPa wind and precipitation indicates that orographic forcing remains the primary precipitation mechanism, while the consistent relationship between the depth of the trough and meridional wind indicates that the relationship between orographic forcing and WWD is unchanged, despite their reduced intensities in spring.

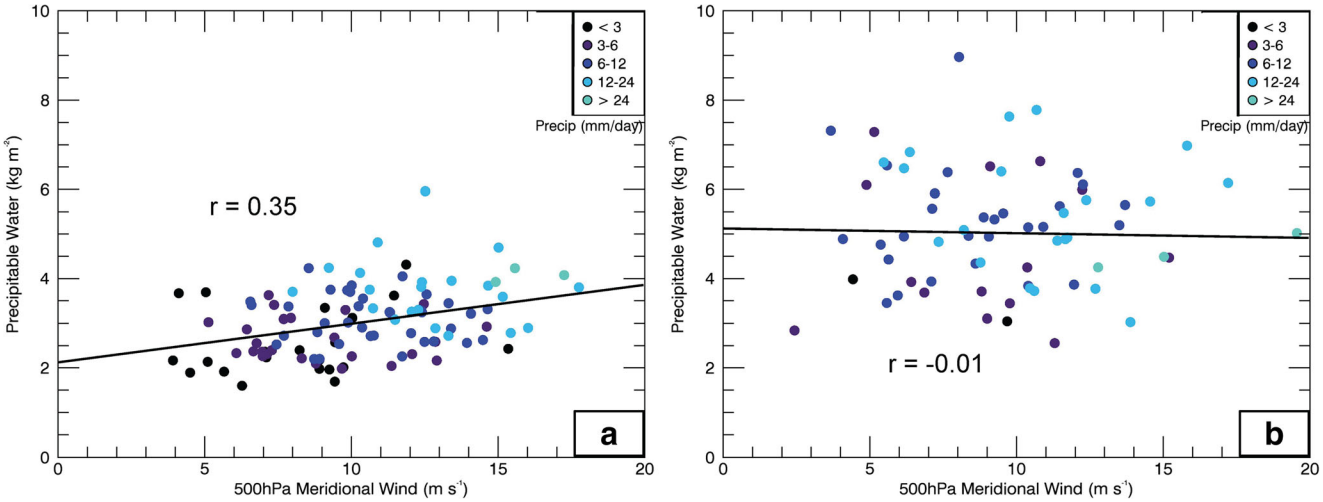

Fig. 12 Regression of 500-hPa meridional wind and precipitable water in the Karakoram region for westerly disturbances in the months of DJF (**a**) and MA (**b**), 1979–2013. *Color* indicates the amount of precipitation received in the Karakoram on the maximum precipitation day during each event

Furthermore, a similar correlation matrix using TRMM precipitation for 50 WWD events in the December through February period and 29 in March and April, 1998–2013 (not shown), displays an even larger reduction in the correlation between precipitable water and precipitation from mid-winter to spring, but no reduction in the correlation between 500-hPa meridional wind and precipitation.

These analyses give additional evidence that orographic precipitation during WWD events occurring from December through February is strongly dependent on moisture that is advected by cyclonic winds associated with the disturbance, while March and April events are characterized by a strong dependence on cross-barrier wind but a weakened relationship with moisture anomalies. By tracking individual WWD events, we are able to illustrate that dynamical forcing alone does not determine precipitation quantity. The fact that there is a significant correlation between precipitable water and precipitation, even in spring when the relationship is considerably weaker, indicates that moisture advection toward the KH, both related to and independent of these events, is an important component of regional precipitation. Moving forward, analysis of variability in WWD-generated KH precipitation should account for large-scale processes including tropical/extratropical interactions, which affect the amount of precipitable water over the Indian subcontinent, and undergo significant modification by global modes of atmospheric variability.

Table 1 Correlation matrix of westerly disturbance 500-hPa geopotential height anomaly at the trough center, Karakoram/western Himalaya precipitation, 500-hPa meridional wind, and precipitable water during 110 independent events occurring December through February (black) and 66 events occurring in March and April (red), 1979–2010. Bold values indicate significance

r	H5	V5	PW	Cp
H5	1	**0.43**	0.03	**0.41**
V5	0.45	1	**0.35**	**0.65**
PW	0.08	0.02	1	**0.57**
Cp	0.37	0.49	0.28	1

H5 depth of 500-hPa geopotential height anomaly at track center, V5 500-hPa meridional wind over the Karakoram, *PW* precipitable water over the Karakoram, *Cp* CFSR precipitation over the Karakoram

8 Conclusions

The objective of this research was to investigate WWD within a framework that facilitated both the observation of individual events and the creation of a large database with information specific to each recorded event. Using CFSR, we created a WWD tracking method based on the presence of upper-level troughs, which are characteristic features of these events. This enabled both the recording of attributes of the disturbances as they moved and evolved and the simultaneous recording of variables related to precipitation in the western Himalaya/KH. The benefit of our wave-tracking methodology over existing cyclone-tracking techniques is specific to regions of high topography and, in our analysis of WWD, gave a unique perspective of the relationship between transient systems and precipitation within our region of interest. Though we do not perform a comprehensive comparative analysis between our methodology and existing extratropical cyclone-tracking techniques, such as those described in Neu et al. (2013), our Northern Hemisphere track densities compare well to the established work of Hoskins and Hodges (2002), which also identified mid-latitude disturbances at the 500-hPa level, and Syed et al. (2010) with a specific focus on high mountain Asia.

Between 1979 and 2013, we observed more than 600 WWD events, 209 of which occurred proximal to the KH (60–75° E, 25–40° N), in a region identified by Cannon et al. (2014) as intimately linked to KH precipitation. The relationship between the dynamics of the identified systems and KH precipitation was investigated with the original goal of identifying multiannual changes in WWD that are indicative of long-term regional climatic variability with significant consequences for KH hydrology. There is much interest in relating variability in the region's hydrometeorology to seasonal snowpack changes (Tahir et al. 2011) and even regional glacier behavior (Kapnick et al. 2014), and better understanding the KH's primary climatic influence is one of many important components in this area of research. Though trends in WWD activity were not discernable, we illustrate the complex relationships between WWD, the mechanisms that drive orographic precipitation in the KH, and how these relationships transform over the course of the winter season.

A significant change from 1979 to 2013 in the number of WWD events affecting the KH was indeterminable from CFSR. We observed there to be an average of 5–6 WWD events in this region per year, with large interannual variability that is likely attributable to teleconnections with global modes of atmospheric variability (Barros et al. 2006; Syed et al. 2006; Yadav et al. 2010; Cannon et al. 2014). In this work, we observed large variability in dynamics and precipitation between individual WWD according to a variety factors. The unique benefit of our tracking method over Eulerian statistics is to facilitate the investigation of precipitation exclusively associated with WWD events and to specifically observe the intensity of these events as identified by upper-level trough depth. This approach allowed for the direct relation of WWD intensity to the mechanisms that drive orographic precipitation in high mountain Asia as well as to each event's respective precipitation total.

The 500-hPa geopotential height anomalies at the WWD center, precipitable water in the KH, 500-hPa meridional wind in the KH, and precipitation in the KH were analyzed for 209 WWD in our region of interest for winter seasons 1979–2013. Unsurprisingly, the depth of the 500-hPa anomaly at the center of the trough and the 500-hPa meridional wind were significantly correlated. Deeper WWD manifested an intensified pressure gradient, thus enhancing the geostrophic wind. The 500-hPa meridional wind during these events was also significantly correlated to precipitation, as orographic lifting is the primary determinant of KH precipitation. On the east side of the disturbance, cyclonic winds produce southerly flow, which advects moisture from the tropics and drives it against KH topography. This relationship between the depth of WWD, the strength of the wind, and the amount of precipitation was observed to change over the course of the winter season. In December, January, and February (DJF), when the temperature gradient across the Northern Hemisphere is strongest, the subtropical jet is at a maximum and is positioned at the same latitude as the Himalaya (Krishnamurti 1961; Holton 2004). Consequently, WWD occurring during DJF were observed to have deeper geopotential height anomalies and higher wind speeds. Upper-level divergence aids large-scale convection, and mechanical forcing of precipitation due to orographic lifting is strongest during these events. Contrastingly, during March and April (MA), the jet has shifted north of the Tibetan Plateau and geopotential height anomalies are shallower, implying weaker winds. However, the Indian subcontinent is considerably warmer than during DJF, and atmospheric moisture content has increased due to increased saturation vapor pressure (Holton 2004). Though WWD in MA are not as dynamically intense, weaker orographic forcing is compensated by the warmer, moister, and less stable conditions, in which orographic precipitation occurs more readily. This illustrated that dynamically weak WWD can thereby produce heavy precipitation events through the enhancement of available moisture, which can be associated with, or independent of, the WWD event, and further exemplifies the complex relationship between WWD and precipitation in the KH.

In addition to seasonal changes in the relationship between WWD and KH precipitation, teleconnections have a strong effect on differences in precipitation produced by WWD occurring at the same time of the year. It is likely that WWD-associated precipitation is highly dependent on a number of factors that are often regulated by global modes of atmospheric variability, including tropical-extratropical interactions and consequent changes in available moisture. Differences between individual WWD precipitation events in the high mountain Asia are therefore modulated by the Madden-Julian Oscillation (Barlow et al. 2005; Hoell et al. 2013), El Niño Southern Oscillation (Syed et al. 2006; Yadav et al. 2010), and the North Atlantic Oscillation/Arctic Oscillation (Gong et al. 2001; Wu and Wang 2002a, b; Yadav et al. 2009; Syed et al. 2010; Filippi et al. 2014). WWD are affected by complex nonlinear relationships throughout the global atmosphere, which significantly alter the dynamics that drive precipitation. Consequently, precipitation totals are dependent on much more than just the strength of the disturbance and should be analyzed accordingly, as was done in this work.

By investigating an inclusive perspective of WWD, which accounts for the dynamics of the systems, how they change across seasons, and how they interact with the background atmosphere, we have improved our understanding of the factors that influence KH precipitation. Moving forward, this creates a basis by which we may better comprehend how a changing climate will affect WWD and, consequently, winter precipitation in high Asia's mountains. This undoubtedly augments our understanding of recent climatic conditions in the region and will improve our ability to project into future decades while minimizing uncertainty with respect to Asia's water resources.

Acknowledgments This research was supported by the Climate and Large-scale Dynamics Program, from the National Science Foundation (NSF award-AGS 1116105) and by NASA Headquarters under the NASA Earth and Space Science Fellowship Program (Grant Number 13-EARTH13F-26). The CFSR data used in this research were developed by NOAA's National Centers for Environmental Prediction (NCEP) and provided by NCAR. TRMM data were acquired by an international joint project sponsored by the Japan National Space Development Agency (NASDA) and the U.S. National Aeronautics and Space Administration (NASA) Office of Earth Science. The authors would also like to thank Dr. Bodo Bookhagen for his help throughout this project.

References

Akperov MG, Yu M, Bardin E, Volodin M, Golitsyn GS, Mokhov II (2007) Probability distributions for cyclones and anticyclones from the NCEP/NCAR reanalysis data and the INM RAS climate model. Izv Atmos Oceanic Phys 43:705–712

Anders AM, Roe GH, Hallet B, Montgomerey DR, Finnegan NJ, Putkonen J (2006) Spatial patterns of precipitation and topography in the Himalaya. Geol Soc Am Spec Pap 398:39–53

Archer DR, Fowler HJ (2004) Spatial and temporal variations in precipitation in the Upper Indus Basin, global teleconnections and hydrological implications. Hydrol Earth Syst Sci 8:47–61

Barlow M, Wheeler M, Lyon B, Cullen H (2005) Modulation of daily precipitation over southwest Asia by the Madden-Julian oscillation. Mon Weather Rev 133:3579–3594

Barros AP, Joshi M, Putkonen J, Burbank DW (2000) A study of the 1999 monsoon rainfall in a mountainous region in central Nepal using TRMM products and rain gauge observations. Geophys Res Lett 27:3683–3686

Barros AP, Chiao S, Lang TJ, Burbank D, Putkonen J (2006) From weather to climate—seasonal and interannual variability of storms and implications for erosion processes in the Himalaya. Geol Soc Am Spec Pap 398:17–38

Benestad RE, Chen D (2006) The use of a calculus-based cyclone identification method for generating storm statistics. Tellus 58A:473–486

Bhutiyani MR, Kale VS, Pawar NJ (2010) Climate change and the precipitation variations in the northwestern Himalaya: 1866–2006. Int J Climatol 30:535–548

Blender R, Fraedrich K, Lunkeit F (1997) Identification of cyclone-track regimes in the North Atlantic. Quart J Roy Meteor Soc 123:727–741

Bolch T, Kulkarni A, Kaab A, Huggel C, Paul F, Cogley JG, Frey H, Kargel JS, Fujita K, Scheel M, Bajracharya S, Stoffel M (2012) The state and fate of Himalayan glaciers. Science 336:310–314

Bookhagen B, Burbank DW (2006) Topography, relief and TRMM-derived rainfall variations along the Himalaya. Geophys Res Lett 33:L08405

Bookhagen B, Burbank DW (2010) Towards a complete Himalayan hydrological budget: the spatiotemporal distribution of snow melt and rainfall and their impact on river discharge. J Geophys Res-Earth 115

Cannon F, Carvalho LMV, Jones C, Bookhagen B (2014) Multi-annual variations in winter westerly disturbance activity affecting the Himalaya. Clim Dyn. doi:10.1007/s00382-014-2248-8

Carlson TN (1998) Mid-latitude weather systems. American Meteorological Society, Boston

Carvalho LMV, Jones C (2001) A satellite method to identify structural properties of mesoscale convective systems based on maximum spatial correlation tracking technique (MASCOTTE). J Appl Meteorol 40:1683–1701

Carvalho LMV, Lavallee D, Jones C (2002) Multifractal properties of evolving convective systems over tropical South America. Geophys Res Lett. doi:10.1029/2001gl014276

Chen QS, Bromwich DH (1999) An equivalent isobaric geopotential height and its application to synoptic analysis and a generalized omega equation in sigma coordinates. Mon Weather Rev 127:145–172

Cohen J, Barlow MA, Kushner P, Saito K (2007) Stratosphere-troposphere coupling and links with Eurasian land-surface variability. J Clim 20:5335–43

Curio J, Maussion F, Scherer D (2015) A twelve-year high-resolution climatology of atmospheric water transport on the Tibetan Plateau. Earth Syst Dyn 6:109–124

Dimri AP, Dash SK (2012) Wintertime climatic trends in the western Himalayas. Clim Chang 111:775–800

Filippi L, Palazzi E, von Hardenberg J, Provenzale A (2014) Multidecadal variations in the relationship between the NAO and winter precipitation in the Hindu-Kush Karakoram. J Clim. doi:10.1175/JCLI-D-14-00286.1

Gardelle J, Berthier E, Arnaud Y (2012) Slight mass gain of Karakoram glaciers in the early twenty-first century. Nat Geosci 5:322–325

Gong DY, Wang SW, Zhu JH (2001) East Asian winter monsoon and Arctic Oscillation. Geophys Res Lett 28:2073–2076

Grumm RH, Hart R (2001) Standardized anomalies applied to significant cold season weather events: preliminary findings. J Forecast 16: 736–754

Hanley J, Caballero R (2012) Objective identification and tracking of multicentre cyclones in the ERA-Interim reanalysis data set. Quart J Roy Meteor Soc 138:612–625

Hatwar HR, Yadav BP, Rama Rao YV (2005) Prediction of western disturbances and associated weather over western Himalayas. Curr Sci India 88:913–920

Hewitt K (2005) The Karakoram anomaly? Glacier expansion and the "elevation effect", Karakoram Himalaya. Mt Res Dev 25:332–340

Hewson TD, Titley HA (2010) Objective identification, typing and tracking of the complete life-cycles of cyclonic features at high spatial resolution. Meteorol Appl 17:355–381

Hoell A, Barlow M, Saini R (2013) Intraseasonal and seasonal-to-interannual Indian Ocean convection and hemispheric teleconnections. J Clim 26:8850–8867

Hoell A, Funk C (2013) The ENSO-related west Pacific sea surface temperature gradient. J Clim 26:9545–9562

Hodges KI (1995) Feature tracking on the unit-sphere. Mon Weather Rev 123:3458–3465

Holton JR (2004) An introduction to dynamic meteorology. Elsevier, Burlington

Hoskins BJ, Ambrizzi T (1993) Rossby-wave propagation on a realistic longitudinally varying flow. J Atmos Sci 50:1661–1671

Hoskins BJ, Hodges KI (2002) New perspectives on the Northern Hemisphere winter storm tracks. J Atmos Sci 59:1041–1061

Huffman GJ et al (2007) The TRMM multisatellite precipitation analysis (TMPA): quasi-global, multiyear, combined-sensor precipitation estimates at fine scales. J Hydrometeorol 8:38–55

Immerzeel WW, Droogers P, de Jong SM, Bierkens MFP (2009) Large-scale monitoring of snow cover and runoff simulation in Himalayan river basins using remote sensing. Remote Sens Environ 113:40–49

Inatsu M (2009) The neighbor enclosed area tracking algorithm for extratropical wintertime cyclones. Atmos Sci Lett 10:267–272

Jones C, Carvalho LMV, Higgins RW, Waliser DE, Schemm JKE (2004) Climatology of tropical intraseasonal convective anomalies. J Clim 17:2078–2095

Kaab A, Berthier E, Nuth C, Gardelle J, Arnaud Y (2012) Contrasting patterns of early twenty-first-century glacier mass change in the Himalayas. Nature 488:495–498

Kapnick SB, Delworth TL, Ashfaq M, Malyshev S, Milly PCD (2014) Snowfall less sensitive to warming in Karakoram than in Himalayas due to a unique seasonal cycle. Nat Geosci 7:834–840

Keable M, Simmonds I, Keay K (2002) Distribution and temporal variability of 500 hPa cyclone characteristics in the Southern Hemisphere. Int J Climatol 22:131–150

Kew SF, Sprenger M, Davies HC (2010) Potential vorticity anomalies of the lowermost stratosphere: a 10-yr winter climatology. Mon Weather Rev 138:1234–1249

Krishnamurti TN (1961) The subtropical jet stream of winter. J Meteorol 18:172–191

Lang TJ, Barros AP (2004) Winter storms in the central Himalayas. J Meteorol Soc Jpn 82:829–844

Lionello P, Kalan F, Elvini E (2002) Cyclones in the Mediterranean region: the present and the doubled CO_2 climate scenarios. Clim Res 22:147–159

Lu N, Qin J, Gao Y, Yang K, Trenberth KE, Gehne M, Yunqiang Z (2014) Trends and variability in atmospheric precipitable water over the Tibetan Plateau for 2000-2010. Int J Climatol. doi:10.1002/joc.4064

Maussion F, Scherer D, Molg T, Collier E, Curio J, Finkelnburg R (2014) Precipitation seasonality and variability over the Tibetan Plateau as resolved by the High Asia Reanalysis. J Clim 27:1910–1927

Murray RJ, Simmonds I (1991) A numerical scheme for tracking cyclone centers from digital data part I: development and operation of the scheme. Aust Meteorol Mag 39:155–166

Neu U et al (2013) IMILAST a community effort to intercompare extratropical cyclone detection and tracking algorithms. Bull Am Meteorol Soc 94:529–547

Norris J, Carvalho LMV, Jones C, Cannon F (2014) WRF simulations of two extreme snowfall events associated with contrasting extratropical cyclones over the Himalayas. J Geophys Res. doi:10.1002/2014JD022592

Palazzi E, von Hardenberg J, Provenzale A (2013) Precipitation in the Hindu-Kush Karakoram Himalaya: observations and future scenarios. J Geophys Res-Atmos 118:85–100

Ramaswamy C (1956) On the sub-tropical jet stream and its role in the development of large-scale convection. Tellus 8:26–60

Ridley J, Wiltshire A, Mathison C (2013) More frequent occurrence of westerly disturbances in Karakoram up to 2100. Sci Total Environ. doi:10.1016/j.scitotenv.2013.03.074

Roe GH (2005) Orographic precipitation. Annu Rev Earth Planet Sci 33: 647–671

Rudeva I, Gulev SK (2007) Climatology of cyclone size characteristics and their changes during the cyclone life cycle. Mon Weather Rev 135:2568–2587

Saha S et al (2010) The NCEP climate forecast system reanalysis. Bull Am Meteorol Soc 91:1015–1057

Serreze MC (1995) Climatological aspects of cyclone development and decay in the Arctic. Atmosphere Ocean 33:1–23

Simmonds I, Murray RJ, Leighton RM (1999) A refinement of cyclone tracking methods with data from FROST. Aust Meterol Mag 35–49

Simmonds I, Keay K (2000) Mean Southern Hemisphere extratropical cyclone behavior in the 40-year NCEP/NCAR reanalysis. J Clim 13: 873–885

Simmons AJ, Willett KM, Jones PD, Thorne PW, Dee DP (2010) Low-frequency variations in surface atmospheric humidity, temperature, and precipitation: Inferences from reanalyses and monthly gridded observational data sets. J Geophys Res 115:1–21

Sinclair MR (1994) An objective cyclone climatology for the Southern Hemisphere. Mon Weather Rev 122:2239–2256

Singh P, Ramasastri KS, Kumar N (1995) Topographical influence on precipitation distribution in different ranges of western Himalayas. Nord Hydrol 26:259–284

Subbramayya I, Raju ASN (1982) A study of tropospheric wave disturbances over India in winter. Pure Appl Geophys 120:437–452

Syed FS, Giorgi F, Pal JS, King MP (2006) Effect of remote forcings on the winter precipitation of central southwest Asia part 1: observations. Theor Appl Climatol 86:147–160

Syed FS, Giorgi F, Pal JS, Keay K (2010) Regional climate model simulation of winter climate over Central-Southwest Asia, with emphasis on NAO and ENSO effects. Int J Climatol 30: 220–235

Tahir AA, Chevallier P, Arnaud Y, Ahmad B (2011) Snow cover dynamics and hydrological regime of the Hunza River basin, Karakoram Range, Northern Pakistan. Hydrol Earth Syst Sci 15:2275–2290

Trigo IF (2006) Climatology and interannual variability of storm-tracks in the Euro-Atlantic sector: a comparison between ERA-40 and NCEP/NCAR reanalyses. Climate Dyn 26:127–143

Wernli H, Schwierz C (2006) Surface cyclones in the ERA-40 dataset (1958–2001). Part I: novel identification method and global climatology. J Atmos Sci 63:2486–2507

Wu BY, Wang J (2002a) Possible impacts of winter arctic oscillation on Siberian high, the East Asian winter monsoon and sea-ice extent. Adv Atmos Sci 19:297–320

Wu BY, Wang J (2002b) Winter arctic oscillation, Siberian high and East Asian winter monsoon. Geophys Res Lett 29:1–4

Wulf H, Bookhagen B, Scherler D (2010) Seasonal precipitation gradients and their impact on fluvial sediment flux in the Northwest Himalaya. Geomorphology 118:13–21

Yadav RK, Rupa Kumar K, Rajeevan M (2009) Increasing influence of ENSO and decreasing influence of AO/NAO in the recent decades over northwest India winter precipitation. J Geophys Res-Atmos 114

Yadav RK, Yoo JH, Kucharski F, Abid MA (2010) Why is ENSO influencing northwest India winter precipitation in recent decades? J Clim 23:1979–1993